



Inertial focusing of cancer cell lines in curvilinear microchannels

Arzu Ozbey^a, Mehrdad Karimzadehkhoei^a, Nur M. Kocaturk^b, Secil Erbil Bilir^b, Ozlem Kutlu^{c,d}, Devrim Gozuacik^{b,c,d}, Ali Kosar^{a,c,d,*}

^a Faculty of Engineering and Natural Sciences, Mechatronics Engineering Program, Sabanci University, Tuzla, Istanbul 34956, Turkey

^b Faculty of Engineering and Natural Sciences, Biological Sciences and Bioengineering Program, Sabanci University, Tuzla, Istanbul 34956, Turkey

^c SUNUM Nanotechnology Research Center, Sabanci University, Tuzla, Istanbul 34956, Turkey

^d Center of Excellence for Functional Surfaces and Interfaces for Nano-Diagnostics (EFSUN), Sabanci University, Tuzla, Istanbul 34956, Turkey

ABSTRACT

Circulating tumor cells (CTCs) are rare cancer cells, which originate from the primary tumors and migrate to the bloodstream. Separation of CTCs from blood is critical because metastatic CTCs might hold different genomic and phenotypic properties compared to primary tumor cells. In this regard, accurate prognosis and effective treatment methods are necessary. For this purpose, focusing biological particles and cells using microfluidic systems have been implemented as an efficient CTCs enumeration and enrichment method. Passive, continuous, label-free and parallelizable size-dependent focusing based on hydrodynamic forces is preferred in this study to sort cancer cells while avoiding cell death and achieving high throughput. The focusing behavior of MDA-MB-231 (11–22 μm), Jurkat (8–17 μm), K562 (8–22 μm), and HeLa (16–29 μm) was examined with respect to different Reynolds numbers and Dean numbers. The effect of curvature on cell focusing was carefully assessed. The focusing positions of the cells clearly indicated that isolations of MDA cells from MDA-Jurkat cell mixtures as well as of HeLa cells from HeLa-Jurkat cell mixtures were possible by using the curvilinear channels with a curvature angle of 280° at the Reynolds number of 121.

1. Introduction

Metastatic tumors originate from primary tumors and are spread through the lymphatic system or bloodstream to the other parts of the body. Due to some genetic mutations, millions of cells shelter in primary tumors and accomplish maintaining cellular functions such as proliferation. Owing to uncontrolled continuous cell proliferation, primary tumor forms, and some rare cells from this tumor become invasive and are released from the primary tumor and start to circulate through to the bloodstream. Most of these cells so-called “circulating tumor cells (CTCs)” die during circulation in the bloodstream, while only 0.01% of them will likely lead to metastasis [1]. While primary tumors barely cause cancer deaths, metastatic cancers ultimately account for 90% of mortality [2]. Thus, development of isolation or detection methods for CTCs will play an important role in assisting oncologists to accurately interpret cancer characteristics while enhancing effective treatment strategies.

Conventional diagnostic strategies for primary tumors include cancer type and cancer location based evaluation of clinical symptoms and rely on imaging techniques such as Magnetic Resonance Imaging (MRI), Computed Tomography (CT), Magnetic Resonance Spectroscopy (MRS), Positron Emission Tomography (PET), Radiography (X-ray), ultrasonography and tissue biopsy examination under microscope [3]. These techniques are based on the utilization of biomarkers identified

from genomic or proteomic analysis and are able to provide morphological, structural, metabolic and functional information about the tumors [4]. However, these techniques can be used only if the tumor is achieved to a certain size and cannot be applied to identify the presence of tumor in early stages, its aggressiveness as well as its response to therapy. Moreover, even though microscopic evaluation of biopsy material by immunohistochemical staining is able to confirm the origin of cancer, there is a clinical suspicion that cancer may not come directly from the biopsy site. Furthermore, the evaluation of molecular biomarkers is usually performed by using primary tumor tissues but this approach does not take potential diversity and heterogeneity between primary tumor and metastatic lesions into account [5]. Thus, primary tumor sampling cannot offer sufficient information about prognosis and treatment [6]. These problems could be solved using a new diagnostic concept: liquid biopsy requiring isolation of CTCs or cell-free circulating tumor DNA (*catena*) from blood [7]. The detection of CTCs in the peripheral blood of patients with cancer is increasingly investigated as a novel biomarker of tumor's growth dynamics, having the potential to give prognostic information and to predict response to chemotherapy [8].

Besides the fact that CTCs may shed light on the evaluation of the cancer stage and determination of therapeutic techniques, CTCs could possibly provide real-time monitoring of tumor progression as representative biomarkers. Metastatic CTCs may have different genomic

* Corresponding author.

E-mail address: kosara@sabanciuniv.edu (A. Kosar).

<https://doi.org/10.1016/j.mne.2019.01.002>

Received 9 November 2018; Received in revised form 19 December 2018; Accepted 18 January 2019

2590-0072/© 2019 The Author(s). Published by Elsevier B.V. This is an open access article under the CC BY-NC-ND license (<http://creativecommons.org/licenses/by-nc-nd/4.0/>).

and phenotypic information in comparison to primary tumor cells or other CTCs as a result of secondary mutation so-called tumor heterogeneity, which constitutes a significant debate in the literature [9–11]. Molecular and cellular analysis of CTCs could contribute to novel personalized cancer treatments [7,12]. However, the concentration of CTCs was estimated to be 1 to 10 CTCs per 10^7 – 10^9 blood cells [13]. Hence, achieving pure CTCs from the blood is still challenging.

Microfluidic technologies come into play with many advantages over conventional technologies such as the requirement of small sample volume, low-cost production and processing higher sensitivity and improved performance [14,15]. Furthermore, microfluidic technologies also facilitate fabrication of integrative, portable point of care diagnostics devices based on lab on a chip or micro-total-analysis-systems (μ TAS). From the microfluidics point of view, separation principles can be divided into two categories depending on external energy usage: active and passive separation [16]. While active techniques require external forces such as magnetic [17], dielectric [18], and acoustic [19] to separate particles/cells, passive techniques utilize mainly hydrodynamic forces [20]. Passive techniques can be further separated into filtration based, deterministic lateral displacement based and inertia-based ones [21]. Noticeably, active techniques provide more accurate results yet are limited by the low throughput, integration of complex components and expensive production or process requirements. Several recent microfluidics cell sorting/isolation reviews can be found in the literature to better understand separation characteristics and physics [22–34].

Liquid biopsy requires isolation of CTCs from the blood followed by single cell analysis. Among the various CTC isolation methods, inertial microfluidics is one of the most appealing size-based isolation phenomena particularly because of its high throughput, easy-to-operate and cheaper nature. However, as the other size-based methods, the main deficiency of the inertial microfluidics is low purity because of the size overlapping of the blood cells and CTCs. At this point, understanding the physics behind the focusing behavior of cells is critical to be able to design novel microchannels to increase the isolation efficiency and purity of CTCs. Recently, the behavior of rigid particles, cancer cells, CTCs or blood cells as well as isolation efficiency of different cell types or particles have been investigated using various types of channel geometries including straight [35–37], spiral [38–42], serpentine [43–48], and straight channel with contraction-expansion arrays [49–51] in inertial microfluidics. However, focusing behavior of the cancer cells in a serpentine channel has not attracted as much attention as the other types.

In this study, continuous, high throughput, label-free and parallelizable size-based cell sorting was performed in symmetrically curved channels by taking the advantage of inertial microfluidics and Dean flow physics while avoiding cell death or damage. The purpose is to understand the curvature effect as well as to achieve an efficient cell focusing in the curvilinear microchannels. Cell focusing behavior for human cancer subtypes from cell lines with diverse biological and biophysical properties was assessed at different flow rates by taking the cell viability and average size of the cells into consideration. The forces acting on these human cancer cell lines alter depending on their 3D location, yet, the concomitant effect is still unknown. After the determination of the optimum parameters to enrich the circulating tumor cell lines, focusing behavior of MDA-MB-231, Jurkat, K562, and HeLa were examined in detail at various Reynolds numbers and Dean numbers. This study has the potential to provide a contribution to the literature in this regard. The assessment of cancer cell migration and equilibrium positions of these cells will lead to the design of futuristic microfluidic innovations for precise detection and diagnosis of cancer in point of care devices with lower costs.

2. Method

2.1. COMSOL modelling

For analyzing the fluid flow inside the microchannel, and acquiring the cross-sectional velocity profiles, COMSOL Multiphysics 5.2 software (COMSOL Inc., Burlington, MA) was used in this study (For the details, see Supp. Info, Text-S2).

2.2. Device fabrication

The PDMS (polydimethylsiloxane) microchannels were fabricated by using the standard soft lithography technique based on our previous study [52]. The details of the technique can be found in Supp. Info., Text S3.

2.3. Cell culture/sample preparation and viability assay

Human breast adenocarcinoma cell line MDA-MB-231 (11–22 μ m), human acute T lymphocyte leukemia cell line Jurkat (8–17 μ m), human chronic myelogenous leukemia cell line K562 (8–22 μ m), and human cervix adenocarcinoma cell line HeLa (16–29 μ m) were used in this study. MDA-MB-231 and HeLa cells were maintained in DMEM high glucose medium (PAN Biotech, P04–03500); Jurkat and K562 cells were maintained in RPMI 1640 medium (Gibco, 31,870–025) in a 5% CO₂-humidified incubator at 37 °C. Culture media were supplemented with 10% heat-inactivated fetal bovine serum (Biowest, S1810–500), antibiotics (50 units/mL penicillin and 50 g/mL streptomycin; Gibco, 15,140–122), and L-glutamine (2 mM, Gibco, 25,030–024). Additionally, MDA-MB-231 media was supplemented with $1 \times$ non-essential amino acids MEM-NEAA solution (Gibco, 11,140,035). The cells were split in every 2 days. Since MDA-MB-231 and HeLa cells are adherent cell lines, Trypsin EDTA Solution A, 0.25%–0.02% (Biological Industries, B103–050-1A) was used to detach cells. 1/10 of the detached cells were inoculated in fresh media. Jurkat and K562 are suspension cell lines. Therefore, 1/10 of their total culture were directly inoculated to fresh media without trypsin treatment.

The cells were fluorescently stained by using DILC18(3) (Life Technologies, D3911). Stock dye solution (2.5 mg/mL) was prepared in Dimethyl Sulfoxide (DMSO) (Santa Cruz, cs-358,801). The cells were re-suspended in PBS (Gibco, 20,012–019) containing 3% FBS in 1,000,000 cells/mL concentration. Stock dye was added in a ratio of 5 μ L/mL of the cell suspension. HeLa, MDA-MB-231, and K562 cell lines were incubated with the dye for 20 min, while Jurkat cell line was incubated for 5 min at 37 °C. Then, the cells were washed with 1 mL PBS at least for 10 times until the supernatant became completely clear. The final number of the cells was adjusted to 150,000 cells/mL by resuspending them in PBS containing 3% FBS. Lastly, the whole suspension was filtered through 70 μ m cell strainer (Falcon, 352,350) prior to its injection to the chip system.

The morphological hallmarks of early stages in cell death are blebbing, cell shrinkage, nuclear fragmentation, chromatin condensation or chromosomal DNA fragmentation. The condensation starts peripherally along the nuclear membrane and during later stages of death, the nucleus further condenses, and finally, it breaks up inside a cell with an intact plasma membrane [53]. This molecular phenomenon can be evaluated by trypan blue exclusion assay (Gibco, 15,250–061). In this assay, loss in membrane integrity was determined by the uptake of the trypan blue dye, to which cells are normally impermeable. For this analysis, HeLa, MDA-MB-231, K562, and Jurkat cells were diluted in $1 \times$ PBS with a 150,000 cells/mL concentration and injected through the chip at the flow rate of 2 mL/min. All cell types were collected immediately after their release from the chip to assess the cell viability after passing through the chip in a biosafety cabinet. The viability was determined as the number of the live cells over the number of total cells counted (the live and dead cells) and the relative percentage of the

control cells at day 0, which were not passing through the chip, was used to represent cell viability without any treatment. To check for the metabolic activity of cells, in other words, activation of programmed cell death, the long-term effect was evaluated by continued culture.

By centrifugation, the cells were isolated from 3% FBS containing PBS solution, re-suspended in their appropriate medium and continued being cultured over the course of 3 days for further viability analyses. Each day, cell images were taken and viability was assessed. For statistical significance, 3 independent experiments ($n = 3$) were performed by injecting different cell suspensions through three different replicas of the same chip for each cell line.

2.4. Device characterization/experimental setup

The cell suspensions were pumped into the microchannels by a 50 mL plastic syringe using a syringe pump (Harvard Apparatus PHD 2000) with an extended range of flow rates. The experiments were started with the lowest flow rate which is 400 $\mu\text{L}/\text{min}$, and after getting video, the flow rate was increased by 100 $\mu\text{L}/\text{min}$. The waiting time at each flow rate was approximately 90 s. This process is continued until the last flow rate, which was 2700 $\mu\text{L}/\text{min}$. Each experiment was repeated for three times. For the details, see Supp. Info, Text-S4.

3. Results and discussion

An illustration of the chip is provided in Fig. 1. Our goal is to apprehend the effect of curvature angle on cell focusing behavior. Since the curvature angle has momentous effects on focusing, the geometry of the microdevice is mainly based on this feature. As the angle of the curvature increases, the Dean flow becomes stronger. Thus, the strength of the secondary flow proportionally depends on the curvature angle.

3.1. Diameter of cells

Due to the size variability of mammalian cells, we measured the sizes of the Jurkat cells, employing to mimic white blood cells (WBCs), and HeLa, MDA-MB231, K562 cells, which were utilized to mimic CTCs following fluorescent staining (Fig. 2a). Although both Jurkat and K562 cells are reflecting white blood cells with similar size, Jurkat cells are commonly used for mimicking white blood cells in CTCs research due to their lymphocytic nature. In addition, a comprehensive analysis of size and elasticity in various cancer cell lines showed that Jurkat cells are the most similar cells to leukocytes [54–56]. It is worth mentioning that the concentration of red blood cells is approximately 10^7 – 10^9 in one mL of blood, and the preliminary red blood cell lysis process is required to eliminate the red blood cells before the isolation of CTCs. Although the concomitant effect of red blood cell lysis process on CTCs is not well understood [51,57], a number of CTCs isolation techniques [58–61] have already included this process in their protocols. After processing, the size distribution of Jurkat cells (mimicking WBCs) in the experiments ranged from 8 μm to 18 μm (Fig. 2b). The determined sizes of CTCs mimicking cells are as follows: MDA-MB231 cells ranged from 11 μm to 22 μm , K562 cells showed approximately a similar pattern ranging from 8 μm to 22 μm , and the size of HeLa cells ranged from 16 μm to 29 μm , which is consistent with recent studies [62–64].

3.2. Viability of cancer cells

The viability of the cells before (Day 0) and after (Day 1, 2 and 3) their release from the microfluidic device was analyzed. Morphological and molecular observations indicate that there was almost no significant side effect of relatively high shear forces on the cell viability, and high viability percentages ($> 94\%$) were achieved (Fig. 3b). Long-term culture analysis of cells showed sufficient recovery of fractions with accomplished cell proliferation and adhesion even for three days after their release from the microfluidic device (Fig. 3a and c).

3.3. Focusing of cancer cells

To better comprehend how inertial lift and Dean drag forces affect the cell motion in curvilinear microchannels, we examined cell focusing in the transition region at various flow rates (400–2500 $\mu\text{L}/\text{min}$). In parallel lines with our previous study [52], where the focusing behavior of polystyrene microparticles with the sizes of 20 μm , 15 μm , and 10 μm was investigated in the same microchannel design, separation potential was observed only in the transition region. Focusing experiments of cancer cell lines of Jurkat (8–17 μm), MDA (11–22 μm), K562 (8–22 μm), and HeLa (16–29 μm) were conducted only in the transition region. Focusing positions and focusing widths of cells are demonstrated in Re_C maps along with representative fluorescent images for a wide range of Reynolds numbers corresponding to different flow rates (Fig. 4).

In wavy (alternating) curvilinear microchannels, due to sudden changes in curvature, Dean flow direction continuously changes in the opposite direction instead of being constant. Because of this continuously change in Dean flow direction, the exact conditions for the steady-state position can be hardly defined [65,66]. Before interpreting the results, it is useful to mention that as we pointed out in the previous study [52], there are two significant facts, which should be taken into account to better analyze the forces acting on the cells: the Dean drag force (F_D) direction, which depends on the vertical position of the cells, and the flow velocity maxima shift, which affects the magnitude of the shear gradient lift force (F_S). Considering cells flowing through in a curvilinear microchannel, the F_D direction cannot be determined unless the cells' vertical position is known since from a cross-sectional perspective the direction of F_D is from the outer wall to the inner wall when the cells are close to the top and bottom walls (below the zero Dean velocity line in the lower half of the channel and above the zero Dean velocity line in the upper half of the channel), while the direction of F_D is from the inner wall to the outer wall when the cells are near the vertical center of the channel (above the zero Dean velocity line in the lower half of the channel and below the zero Dean velocity line in the upper half of the channel). Another Dean flow effect on the behavior of the cell can be seen in the main flow velocity profile. Due to the fact that the velocity profile in straight channels is parabolic, velocity maxima are located at the centerline. Nevertheless, adding curvature to the channel geometry not only results in the creation of the F_D but also changes the velocity maxima location.

The direction and presence of the forces acting on cells dramatically depend on the cell location along the channel. To better understand the force analysis, here we defined three different locations in the channel: 1) upstream of the transition section (Region 1), 2) transition section where A-A' line passes (transition section (TR)), and 3) downstream of the transition section (Region 2) (Fig. 1). According to our findings, different types of the cells exhibit similar trends (in another words at least one of the following events are in common for different types of the cells), such as a wide cell focusing band near the centerline at low Re , a tighter cell focusing stream near the centerline, a sudden defocusing, refocusing near the wall along with the transverse motion, and a second defocusing (Dean mixing). The transverse motion of rigid particles passing through the curved channels was also observed by Gossett et al. [67]. To better explain the physics behind these trends, we defined three distinct cases (Fig. 5).

At low Re ($Re \sim 30$), no focusing line can be observed for Jurkat cell lines. Instead, cells form a wide band near the centerline due to relatively small Dean drag and inertial lift forces (Fig. 4a). Increasing the Re ($Re \sim 83$) results in the formation of a thinner focusing line (focusing width of 35 μm) near the centerline, slightly closer to the W_1 . This focusing line migrates towards the centerline when the flow rate is increased as described in Case I. When cells are in Region 1, where the maxima of the velocity profile are in the half channel near the inner wall, the cells are pushed from the velocity maxima to the outer wall by the horizontal component of the F_S . In this case, the vertical location of

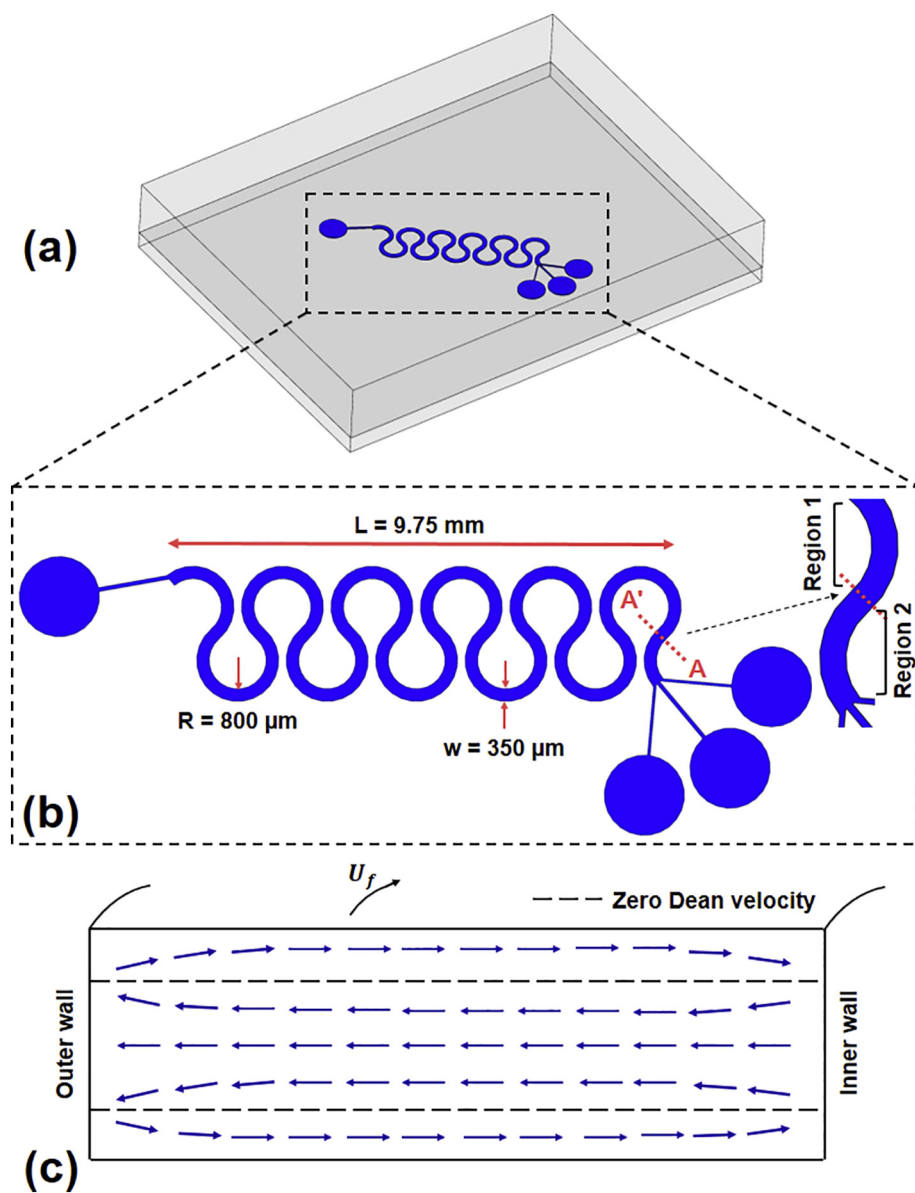


Fig. 1. (a) Schematic of the microfluidic chip (A typical PDMS microfluidics chip consists of one microchannel design with one inlet, and three outlets with a diameter of 1 mm each. The height of the microchannel is 91 μm , while the width and radius of curvature are 350 μm and 800 μm , respectively. The whole chip houses 11 curvilinear geometries, each having the angle of curvature of 280° . The total chip length is 9.75 mm.), (b) Close up view of the curvilinear microchannel with dimensions. (A-A' cross section is the transition cross section), and (c) Dean vortices at the cross-section of the microchannel. From a cross-sectional view, two vortices track the lane from the inner wall to the outer wall, parallel to the z-axis in the middle of the microchannel. Since these two vortices are counter-rotating, the direction of the Dean flow is from the outer wall to the inner wall near the top and bottom walls. Due to the sudden rotational change, the inner wall becomes the outer wall and vice versa. Hence, in the transition section, the walls cannot be defined as outer and inner walls. The A- and A'-sides of A-A' cross-section at the transition section were labeled as W_1 and W_2 , respectively.

the cells is hypothesized to be above and below the zero Dean velocity line in the upper and lower halves of the microchannel, respectively, and the direction of the F_D is from the outer wall to the inner wall (Fig. 5a). Thus, the F_D balances the F_S , where cells go along the centerline. By further moving the cells to the transition section (Section TR), due to the formation of the velocity maxima at the centerline, the lift coefficient will be zero, leading to the lack of the F_S at this section. Furthermore, since the direction of the curvature suddenly changes, (as the inner wall becomes the outer wall and vice versa), the effect of curvature can be neglected in this section, hence, the F_D can be ignored. In other words, in this section, neither Dean drag force nor inertial forces are dominant, thus, the cells follow the streamlines until the velocity maxima are redistributed (Fig. 5b). After passing the transition section, due to change in the direction of the channel curvature, the direction of the forces shifts to the opposite direction, whereas the velocity maxima move towards the inner wall again. At this region (Region 2), the horizontal component of the F_S acts on the cells from velocity maxima to the outer wall (opposite to the F_D) (Fig. 5c).

A sudden defocusing behavior is observed while increasing Re to Re ~ 114 (Fig. 4). Not only horizontal but also vertical components of the F_S decrease because an increase in the flow velocity results in a decrease

in the lift coefficient [68]. As a consequence of crossing the zero Dean velocity line, cells move towards the vertical center of the channel, where the direction of F_D reverses. Thereupon, both the F_S and F_D act on the cells towards the outer wall at Regions 1 and 2, while F_S alone pushes cells towards the W_2 at transition section resulting in a defocusing behavior.

Following that, with a further increase in Re, a transverse motion of focusing cell line is observed (Case III): cells do not migrate along the essential flow stream but perpendicular to this stream as they move closer to the W_2 at the transition section instead of remaining at the channel center (Fig. 4). This behavior implies that the cell migration velocity, U_C , is perpendicular to the average fluid velocity, U_f . When Jurkat cells are in Region 1, where the velocity maxima are in the inner half of the channel, cells are pushed towards the outer wall by the influence of both F_D and F_S (Fig. 5g). When cells arrive to the section TR, they are already close to the W_2 from the previous position. Since the velocity maxima are near the centerline, a F_S acts on cells from velocity maxima to W_2 , meanwhile, a wall induced lift force (F_w) comes into play, this time because of the cells' position, and balances the F_S resulting in a focusing cell line near the transition section (Fig. 5h). When the cells reach the Region 2, the directions of both F_D and F_S change to

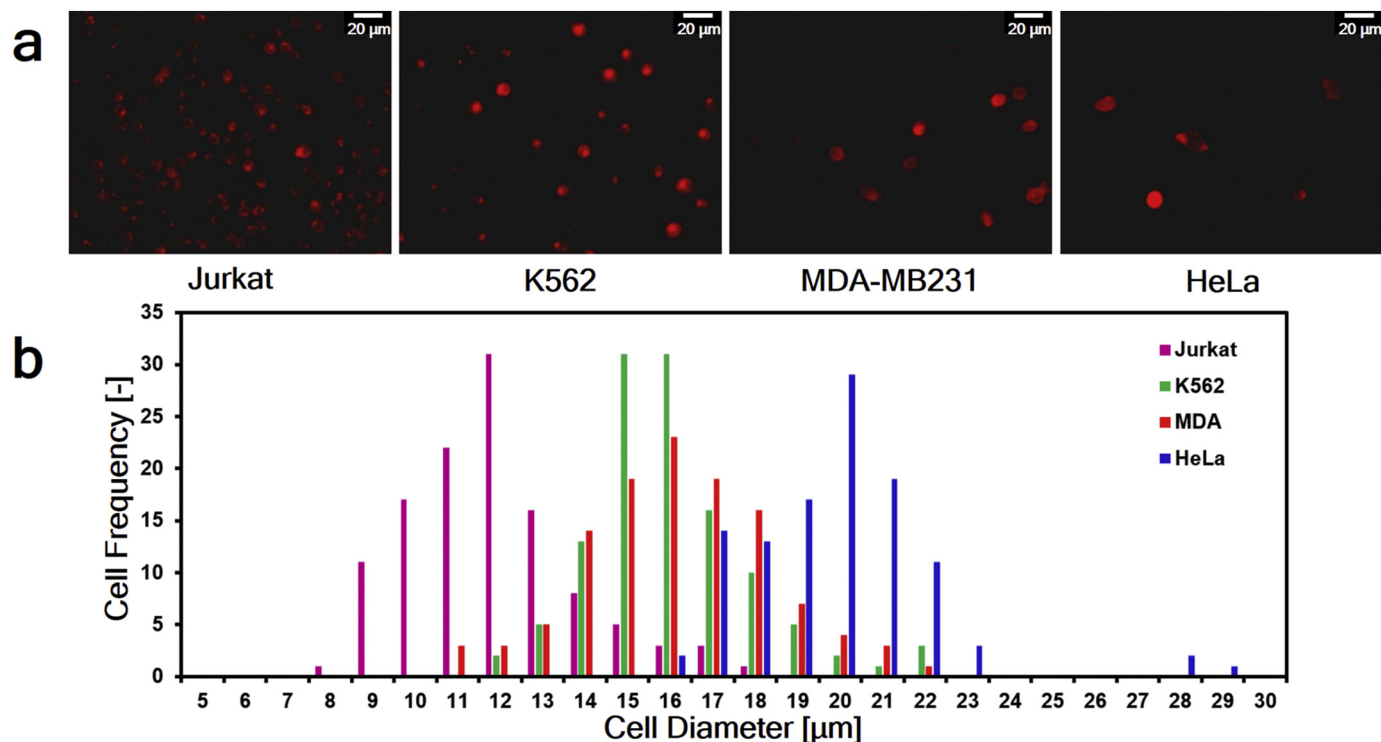


Fig. 2. (a) Visual images of the cells after staining, and (b) Size distribution of the cells. After processing, the size distribution of Jurkat cells (mimicking WBCs) in the experiments ranged from 8 µm to 18 µm. The determined sizes of CTCs mimicking cells are as follows: MDA-MB231 cells ranged from 11 µm to 22 µm, K562 cells showed approximately a similar pattern ranging from 8 µm to 22 µm and the size of HeLa cells ranged from 16 µm to 29 µm, which is consistent with recent studies [62–64].

the opposite direction (the inner wall becomes the outer wall and vice versa) pushing cells towards the centerline, where the shear area is larger (Fig. 5i). A further increase in Re_C to 144 results in a mixing effect of the cells because F_D overcomes F_S . The lift coefficient decreases with the increasing flow velocity [68], and at some point, the F_D becomes greater than the F_S .

Likewise, MDA cell lines initially focus in a wide band (around 130 µm) near the centerline at low Re ($Re \sim 30$) (Fig. 4) due to relatively small inertial lift and Dean drag forces combined with the low flow velocity. With an increase in the Re ($Re \sim 83$), a single cell streak with a width of almost twice the diameter of a single cell near the centerline is seen at the transition section, where the streak is slightly closer to the W_1 at the transition section. Comparing the Jurkat and MDA cells, it can be seen (Fig. 4) that the Jurkat cells move closer to the W_1 than MDA cells at low Re ($Re \sim 38$). Without a full evaluation, this behavior of the cells is unexpected at first sight, because the F_S and F_D change with a_p^3 and a_p , respectively. Therefore, the presumed lateral position of medium size cells is closer to the centerline than large ones. By taking the 3D position of the cells and scaling F_S with the cells' vertical position into account, it can be predicted that the large cells are pushed to the bottom and top walls of the channel, where F_D is stronger. Due to dominance of F_D on large cells at the bottom and top walls and closer position of medium cells to the zero Dean velocity line, F_D acting on the large cells is greater in comparison with that on the medium size cells so that large cells move closer to the center of the channel than the medium size cells.

With a further increase in Re ($Re > 114$), the MDA cell stream slightly migrates towards the W_2 , before the sudden defocusing (Case II). When cells are in the Region 1, cells are close to the top and bottom walls, where the directions of F_S and F_D are from the inner wall to the outer wall and from the outer wall to the inner wall, respectively (Fig. 5d). An increase in flow rate results in an increase in both of F_S and F_D . However, F_S increases more than F_D ($F_S \propto U_f^2$, $F_D \propto U_f^{1.63}$) leading to migration of MDA cell line towards the outer wall in this region. This

migration behavior is not clearly seen in Jurkat cell lines, because the size of Jurkat cells is smaller than that of MDA cells and not only horizontal but also vertical component of F_S acting on Jurkat cells is smaller than that on MDA cells at the same flow rate ($F_S \propto a_p^3$). Hence, the vertical position of Jurkat cells approaches to the channel center at lower Reynolds numbers. When cells move to the transition section, where velocity maxima are near the center of the channel, MDA cells are not seen at the centerline now. Therefore, unlike Jurkat cells, F_S is present and pushes cells from centerline to the W_2 . When cells arrive the Region 2, F_D acts on the cells as the counterbalancing force of F_S (Fig. 5e). With a further increase in flow rate, at some point, cells' vertical position alters towards the center of the channel, where F_D acts in the same direction as F_S , leading to a defocusing trend when $Re \sim 129$ (Fig. 4). Beyond that, a single cell focusing line is formed near the W_2 in Region 2 along with a transverse motion of the cells along the channel (Case III), where the particles do not follow the essential flow stream but instead migrate perpendicular to this stream. Different from Jurkat cells, Dean mixing behavior is not observed in MDA cells. Because of the larger diameter of the cells, a higher flow rate is required for F_D to become greater than F_S ($F_{S, Jurkat} < F_{S, MDA}$).

No effective single focusing line of K562 cells is observed in this study, possibly due to a wide range of size distribution of the cells (8–22 µm). However, after a careful examination of the intense green areas in Fig. 4, it can be deduced that the behavior of the K562 cells is very similar to that of MDA cells. The most significant factor in cell behavior is the size. However, the average diameter of both cells is very close to each other such that K562 and MDA cells have the average diameter of 16 µm and 17 µm, respectively. With an increase in the Re , the following observations are present for K562 cells: (1) a wide focusing band at low Re ($Re \sim 38$) such that the widest focusing band among all the cells can be seen here, (2) a tighter focusing band near the centerline of the channel ($Re \sim 76$ –91) (Case I), Fig. 5a, (3) defocusing of the cell focusing band ($Re \sim 98$) as a result of transverse motion of the cells, (4) tighter focusing band near the W_2 ($Re \sim$

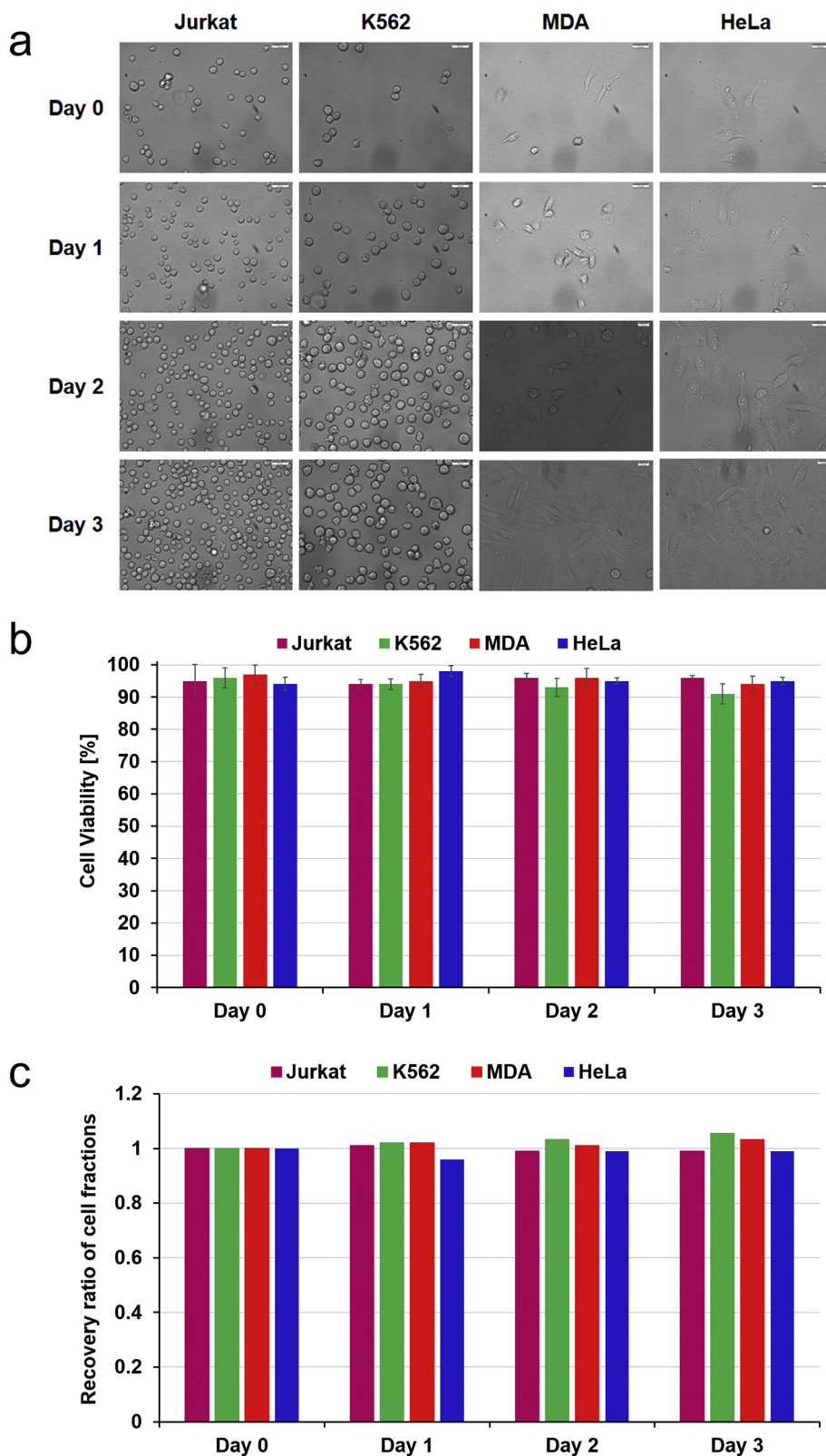


Fig. 3. The viability of the cells was analyzed after their release from the chip, named Day 0. For further viability assays, cultured cells were examined 24, 48 and 72 h after performing the focusing experiments, namely Day 1, Day 2 and Day 3, respectively. (a) The morphological images of Jurkat, K562, MDA, and HeLa cells at day 0, 1, 2 and 3. (b) Cell viability of cells at indicated durations. Data are shown as mean of 3 independent experiments \pm S.D. ($n = 3$). Cells could survive for three days after their release with accomplished cell proliferation and adhesion and exhibited similar viability rates ($> 90\%$) underlying the cell viability in all cell lines which were employed in this study under high shear forces. (c) Recovery ratio of cell fractions. The ratio was determined as the percentage of live cells before fractionation (at day 0) over the percentage of live cells after fractionation (at day 1, 2 and 3).

152–174) (Case III), Fig. 5c, and finally (5) a second defocusing due to dominant F_D ($Re \sim 182\text{--}189$), (Fig. 4).

Due to the larger average diameter of HeLa cells ($F_S \propto a_p^3$, $F_D \propto a_p$), (among all the cell types employed in this study), the smallest width of the initial wide focusing band is observed for HeLa cells when Re is 38 (Fig. 4). The behavior of HeLa cells is somewhat similar to that of MDA cells until Re becomes 129. Beyond that, a sudden defocusing occurs for

MDA cells, whereas the single focusing stream of HeLa cells continues with its migration to the W_2 until $Re \sim 152$ (Case II). In Case II, because of the larger diameters of HeLa cells, again, not only horizontal but also vertical component of F_S acting on HeLa cells is greater than that on MDA cells ($F_S \propto a_p^3$). Therefore, the magnitude of the vertical component of the F_S is sufficient enough to keep HeLa cells below the zero Dean velocity line in the lower half of the channel and above the zero

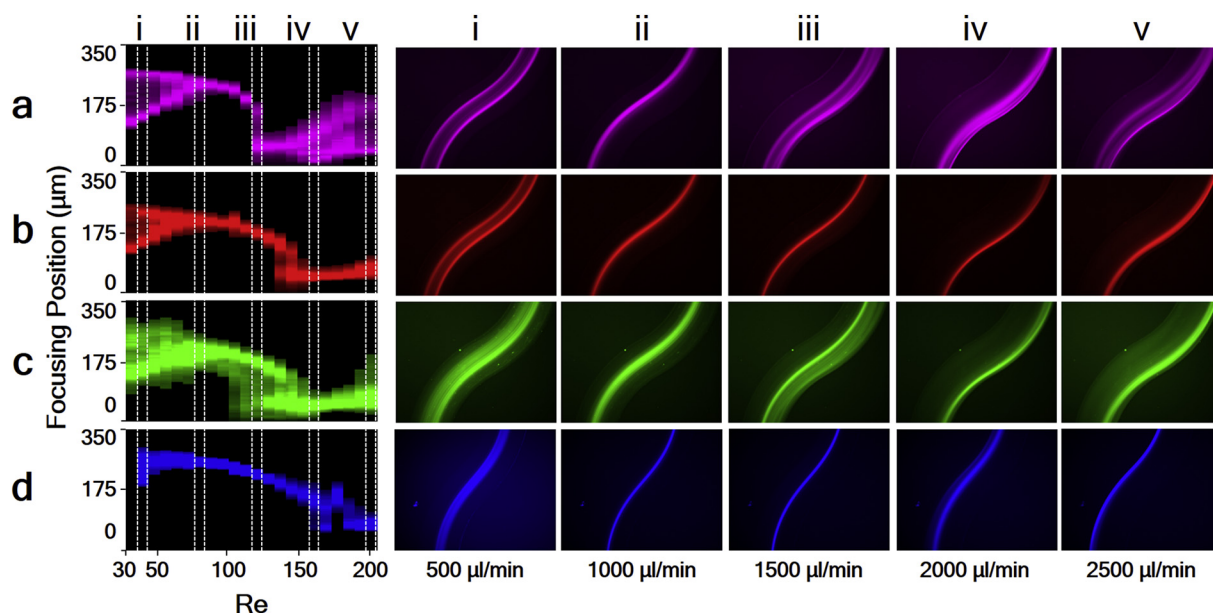


Fig. 4. Re maps at the transition section: (a) Jurkat (magenta), (b) MDA cell line (red), (c) K562 cell line (green), (d) HeLa (blue) cell lines (left column). Cell line streams for different Reynolds numbers corresponding to five selected flow rates between 500 and 2500 $\mu\text{L}/\text{min}$ (i-v) (right columns). The A- and A'-sides of A-A' cross-section at the transition section were labeled as W_1 and W_2 , respectively. The top and bottom of each map are represented as W_1 and W_2 , respectively.

Dean velocity line in the upper half of the channel, while it is not adequate for MDA cells to keep them close to the channel top and bottom walls at $Re \sim 152$.

In Region 1, the direction of F_S is from velocity maxima to the outer wall, whereas the direction of F_D is from the outer wall to the inner wall (Fig. 5d). Because of the fact that F_S and F_D scale with U_f^2 and $U_f^{1.63}$, respectively, a greater F_S compared to F_D causes a migration of single

cell focusing stream towards the outer wall. In the transition section, since cells are not at the centerline anymore, F_S is present and it is the only major force acting on the HeLa cells. However, the focusing stream is not disturbed, probably because of the momentum of the cells. At first glance, it may be confusing that the F_S is present in Case II and not in Case I at the transition section. The reason behind this is that the location of the cells in Case I is not the same as in Case II. When Re is 159,

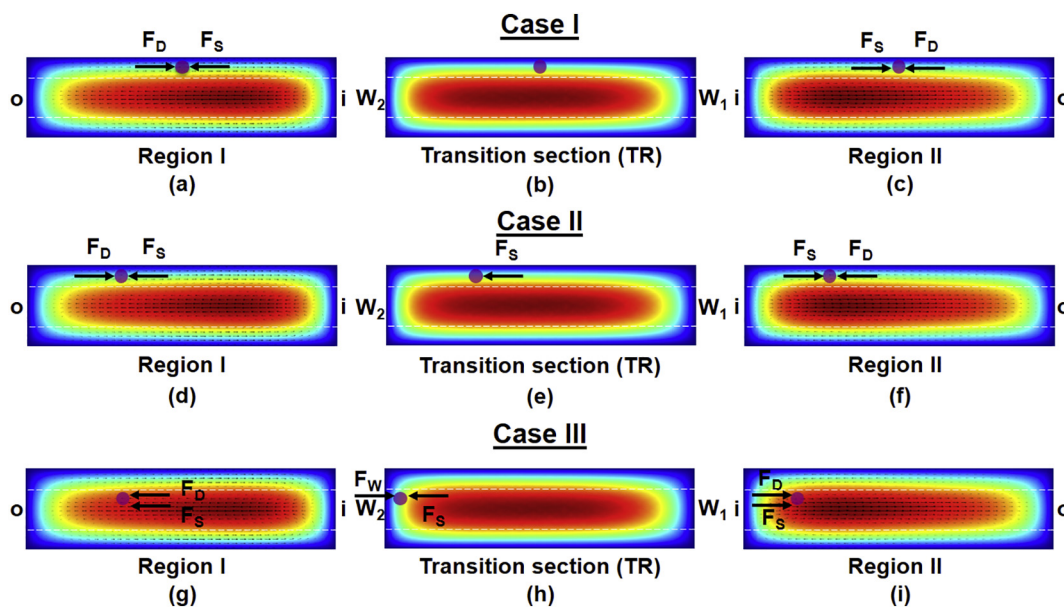


Fig. 5. Forces acting on the cells: Case I) when the cells go along the channel near the centerline before defocusing, Case II) when the cells migrate towards the W_2 before defocusing, and Case III) transverse motion and refocusing near the W_2 at the transition section after defocusing. (Estimated approximate cells positions from a cross-section view of the channel and forces acting on the cells for each case as well as each region and transition section are displayed.) The velocity maxima form near the inner half of the channel in Region 1 and shift to the channel centerline at the transition section (Section TR). Although the inner wall becomes the outer wall beyond the transition section, the velocity maxima again shift to the inner half of the channel in Region 2. Continuously shifting the velocity maxima in the transition sections results in a differential change not only in the horizontal component but also in the vertical component of the F_S . Therefore, the 3D position of the cells continuously changes. This effect amplifies with decreasing cell size because F_S scales with a_p^3 , hence, the vertical component of the F_S will be still sufficient enough for pushing the larger cells above the zero Dean velocity line while smaller cells approach to the vertical center of the channel due to a weaker vertical component of F_S and experience a change in the F_D direction. It is worth mentioning that the direction of the F_S is from the velocity maxima to the channel walls. The A- and A'-sides of A-A' cross-section at the transition section were labeled as W_1 and W_2 , respectively.

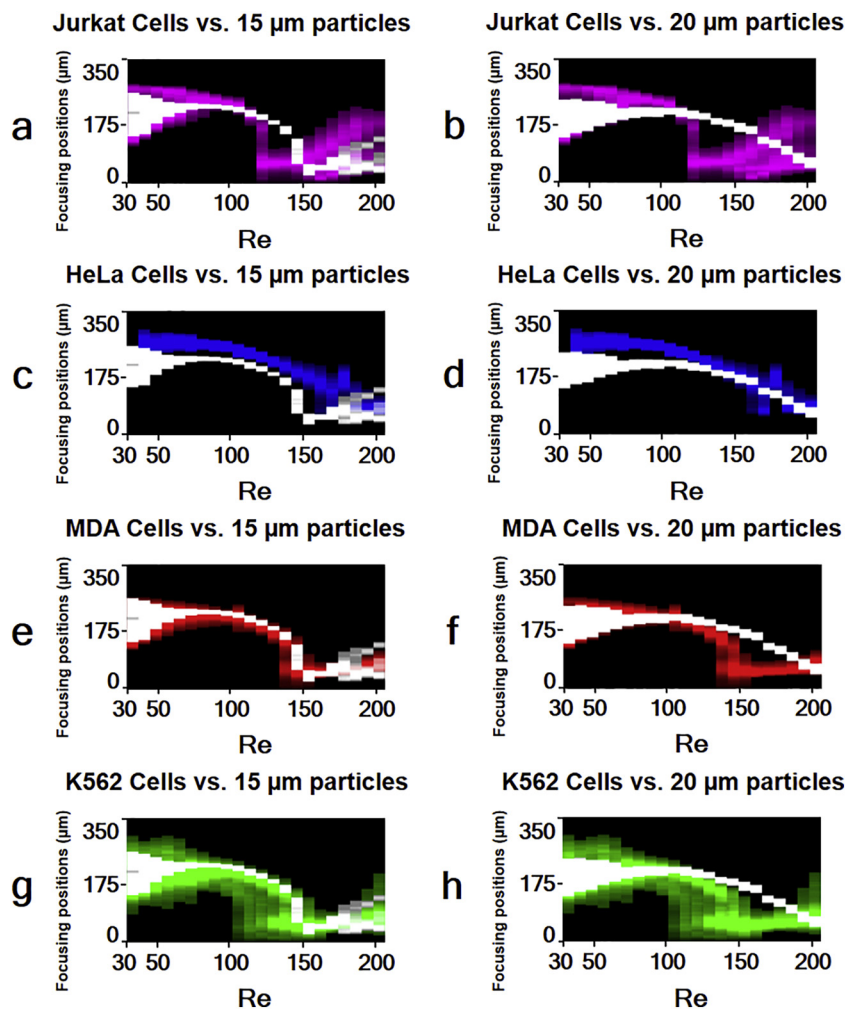


Fig. 6. A comparison between the rigid microparticles (white) and the employed cells, Jurkat cells (magenta), HeLa cells (blue), MDA cells (red), K562 cells (green). (For interpretation of the references to colour in this figure legend, the reader is referred to the web version of this article.)

the HeLa cells are defocused and increasing the Re_C further ($Re > 174$) results in refocusing of cells near the W_2 (Case III). Defocusing occurs at higher Re for these cells compared to the other ones ($Re \sim 159$) because of larger average diameter. In case III, after defocusing, cells approach to the outer wall in the region I under the influence of the combined effect of Dean drag and inertial lift forces (Fig. 5g). Since the cells are already close to the outer wall in the region I, when they arrive the transition section, they are also close to the W_2 . Hence, F_S balances F_W in the section TR (Fig. 5h).

3.4. Comparison between the cells and the particles with 15 and 20 μm diameter

Particle dynamics of polystyrene microparticles with the diameter of 10, 15 and 20 μm was analyzed using the same microchannel configuration in our previous study [52]. To have a better understanding about inertial microfluidics, a comparison of focusing positions of rigid (polystyrene) and elastic (cells) particles is presented in Fig. 6 based on the experimental data of our previous study [52]. Owing to the fact that particles/cells behavior highly depends on the size in inertial microfluidics, our priority on interpreting the results relies on the size proximity between the type of cells and the polystyrene particles. However, due to the fact that no single focusing position of 10 μm particles is observed in our previous study [52], comparison of 10 μm particles with cancer cell lines is found to be unnecessary.

The size distribution of the Jurkat cells is between 8 and 17 μm , and

their average diameter is 12 μm . Since the average diameter of these cells is close to 15 μm rather than 20 μm , the focusing trend of Jurkat cells is more similar to the 15 μm particles (compared to 20 μm particles) as can be seen in Figs. 6a and b. However, the sudden defocusing occurs when Re is 114, while it is observed at $Re \sim 136$ for the 15 μm particles. Additionally, the Dean mixing effect on Jurkat cells is stronger than that on 15 μm particles. It is likely because the average diameter of Jurkat cells is smaller than 15 μm .

Likewise, because the average diameter of HeLa cells (21 μm) is closer to the 20 μm rather than 15 μm , and the size distribution of these cells is in between 16 μm to 21 μm , the focusing trend of the HeLa cells is similar to the 20 μm particles (Fig. 6d). However, the initial wide focusing band of HeLa cells is found to be closer to W_1 compared to the 20 μm particles at low Re . While the sudden defocusing is not observed for 20 μm particles, the focusing stream of the HeLa cells is disturbed when Re is 152.

Since the average diameter of the MDA cells (17 μm) is between 15 μm and 20 μm , the focusing behavior of these cells is seen to be a combination of the 15 μm and 20 μm particles' behavior (Figs. 6e and f). The sudden defocusing observed for 15 μm particles is also seen in the MDA cells. However, Dean mixing is not observed similar to the 20 μm particles. Instead, MDA cells focus near the W_2 at higher Re .

Comparing the behavior of the K562 cells with the 15 and 20 μm particles is rather difficult because a single cell focusing line cannot be observed for K562 cells. It is likely because of the wide range of cell diameter, which is between 8 and 22 μm . Somehow, events like sudden

defocusing, focusing near the W_2 , and Dean mixing are in common with the $15\ \mu\text{m}$ particles.

In addition to shear gradient lift, wall induced lift, and Dean drag forces, the deformability of bio-particles/cells can lead to additional lift forces. Hur et al. studied different particles with different shapes and reported that focusing positions of particles were not affected by the shape of the particles [69]. In contrast to a rigid particle, a deformable particle may have a net lift force leading to particles' lateral migration. Hur et al. and Masaeli et al. showed that above a critical Reynolds number ($Re \sim 50$), particles predominantly adopted preferred equilibrium positions and “tumbling” rotational axis [69,70]. This rotational axis focusing position was found to be independent of cross-sectional shape and mainly dependent on the rotational diameter. During the tumbling motion, when the major axis rotates perpendicular to the wall, the wall induced lift increases substantially due to the closer distance. As a result, the combined force on the particle/cell is higher than that on a sphere of the same volume. Hur et al. experimentally demonstrated that the direction of deformability-induced lift force is towards the center (in Poiseuille flow) [71]. As the deformability induced lift force increases, cells shift towards the channel center in straight channels. This effect is not clearly detected in our study. In fact, comparing the behavior of cells with rigid particles from the theoretical point of view is challenging since the standard deviation of the size range of commercially available particles is rather small compared to that of the cells.

3.5. Focusing positions

The overlaid fluorescent images and the focusing positions graphs are illustrated in Fig. 7. The results indicate that separation of K562 cells from Jurkat cells is not possible, because no effective single cell focusing line of K562 cells is achieved (Fig. 4). The optimum separation potential is achieved for the Jurkat and MDA cells when Re is 121 at the transition section in the symmetric curvilinear channel (with the curvature angle of 280°) (Fig. 7a), since MDA cells move near the centerline, while most of Jurkat cells travel near the W_2 . One of the main reasons for different focusing stream locations of these two cells is that the dimensions of the cells are different, and therefore, the directions of the forces acting on the cells are different because of the different vertical positions of the cells. The corresponding distance between the focusing streams of Jurkat and MDA cells is approximately $95\ \mu\text{m}$. In

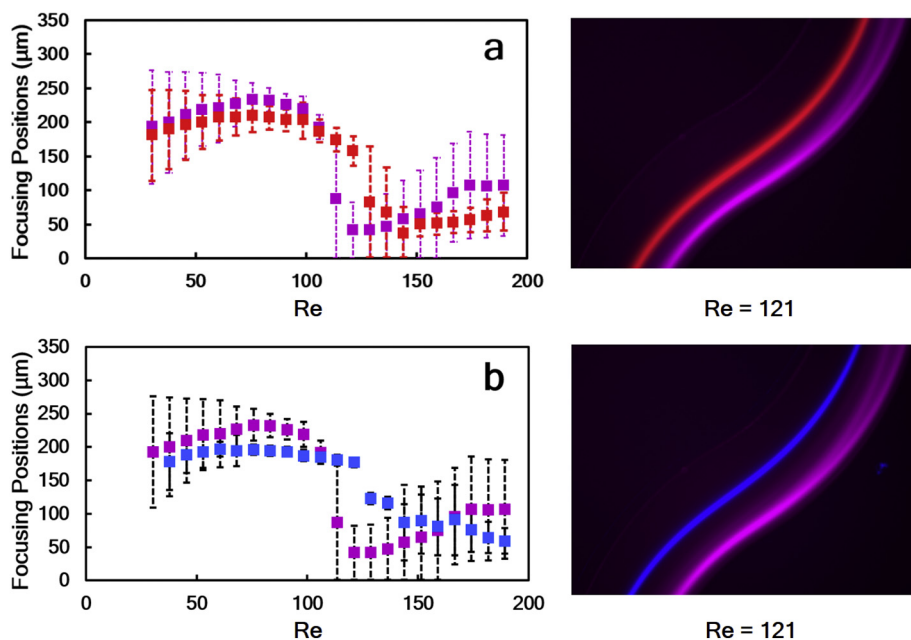


Fig. 7. Focusing positions of the cancer cell lines at the transition region in the curvilinear channel with a curvature angle of 280° for different flow rates (left column), cell streams for optimum Reynolds number (right column) for: a) Jurkat (magenta) and MDA (red), b) Jurkat (magenta), and HeLa (blue) cell lines. Error bars indicate the focusing width. Jurkat cell lines were used to mimic white blood cells, and K562, MDA-MB-231, and HeLa cells were used to mimic circulating tumor cells. (The optimum conditions for cells (between Jurkat and CTCs) were determined based on the measurements of the distance between the cell streams at the given Reynolds number.) (For interpretation of the references to colour in this figure legend, the reader is referred to the web version of this article.)

the same manner, the optimal Reynolds number is found to be 121 for the HeLa and Jurkat cells with a focusing cell stream distance of approximately $105\ \mu\text{m}$.

4. Conclusions

A continuous, high-throughput and parallelizable size-based particle focusing technique was developed in a specific symmetrical curved channel by taking the advantage of inertial microfluidics and Dean flow physics. The inertial focusing behavior of cancer cell lines MDA-MB-231 ($11\text{--}22\ \mu\text{m}$), Jurkat ($8\text{--}17\ \mu\text{m}$), K562 ($8\text{--}22\ \mu\text{m}$), and HeLa ($16\text{--}29\ \mu\text{m}$) in a curvilinear channel with a curvature angle of 280° was investigated in this study.

Our simulation results show that the velocity maxima shift from the inner wall to the centerline and from the centerline to the inner wall again along the channel in the transition section under the influence of Dean flow. Hence, the lateral position of cells is significant when considering the force balance. This study also underlines the significance of the recognition that not only lateral but also vertical positions of cells depend on the flow velocity as well as the cell size, which dramatically alters the force balance on the cells. Comparing bioparticles (cells) with rigid particles, it is foreseen that further comprehensive studies on simulation of the behavior of particles or cells by considering the elasticity or stiffness effect at different flow rates as well as on the effect of size range of particle/cell on their focusing behavior will elicit the reason behind different focusing characteristics.

Our results indicate that separations of the MDA and Jurkat cells (Jurkat cells were used to mimic white blood cells) as well as the HeLa and Jurkat cells can be possible at the transition section of the symmetric curvilinear channels (with curvature angle of 280°) at $Re \sim 121$ since the maximum distances between the Jurkat and MDA cells and Jurkat and HeLa cells were measured as $95\ \mu\text{m}$ and $105\ \mu\text{m}$, respectively, at this Reynolds number. Additionally, this design is compatible with high throughput designs since many parallel channels could be placed in a rather small footprint area. Based on the results of this study, it can be deduced that the isolation of CTCs from vasculature system can be achieved, although further studies should be performed by using patient samples in order to put the current design in clinical context. Because of promising results, we believe that the characterization of rare cells in future studies will lead to better prognosis using CTC isolation from blood.

Acknowledgments

The authors are thankful to Prof. Devrim Gozuacik's lab members from Molecular Biology, Genetics and Bioengineering Program, and Prof. Kursat Sendur from Mechatronics Engineering Program, Sabanci University for their assistance and support, Sabanci University Nanotechnology Research and Applications Center (SUNUM), Faculty of Engineering and Natural Science of Sabanci University (FENS). This work was supported by the Sabanci University Internal Research Grant, No: IACF12-00970, TUBITAK (The Scientific and Technological Research Council of Turkey). N.M.K. and S.E.B. were supported by TUBITAK BIDEB2211 Scholarship for their Ph.D. studies.

Authors contributions

A.O. and A.K. designed the experiments. A.O. and M.K. fabricated the device, performed the experiments, and prepared the figs. N.M.K. and S.E.B. prepared, characterized the samples and performed the viability tests. All the authors reviewed the manuscript.

Appendix A. Supplementary data

This document consists of supporting information about the Working Principle, COMSOL Modelling, Device Fabrication, and Device Characterization/Experimental Setup. Supplementary data to this article can be found online at <https://doi.org/10.1016/j.mne.2019.01.002>.

References

- X. Zhe, M. Cher, R. Bonfil, Circulating tumor cells: finding the needle in the haystack, *Am. J. Cancer Res.* 1 (2011) 740–751.
- G.P. Gupta, J. Massagué, Cancer metastasis: building a Framework, *Cell* 127 (2006) 679–695, <https://doi.org/10.1016/j.cell.2006.11.001>.
- P. Kumar, R. Pawaiya, *Advances in cancer diagnostics*, Braz. J. Vet. 3 (2010) 141–152.
- S. Kumar, A. Mohan, R. Guleria, Biomarkers in cancer screening, research and detection: present and future: a review, *Biomarkers* 11 (2006) 385–405, <https://doi.org/10.1080/1354750060075011>.
- S. Vignot, B. Besse, F. André, J.-P. Spano, J.-C. Soria, Discrepancies between primary tumor and metastasis: a literature review on clinically established biomarkers, *Crit. Rev. Oncol. Hematol.* 84 (2012) 301–313, <https://doi.org/10.1016/j.critrevonc.2012.05.002>.
- C. Wittekind, M. Neid, Cancer invasion and metastasis, *Oncology* 69 (Suppl. 1) (2005) 14–16, <https://doi.org/10.1159/000086626>.
- K. Pantel, C. Alix-Panabières, Real-time liquid biopsy in cancer patients: fact or fiction? *Cancer Res.* 73 (2013) 6384–6388, <https://doi.org/10.1158/0008-5472.CAN-13-2030>.
- K. Pantel, C. Alix-Panabières, Circulating tumour cells in cancer patients: challenges and perspectives, *Trends Mol. Med.* 16 (2010) 398–406, <https://doi.org/10.1016/J.MOLMED.2010.07.001>.
- A.A. Powell, A.H. Talasz, H. Zhang, M.A. Coram, A. Reddy, G. Deng, M.L. Telli, R.H. Advani, R.W. Carlson, J.A. Mollick, S. Sheth, A.W. Kurian, J.M. Ford, F.E. Stockdale, S.R. Quake, R.F. Pease, M.N. Mindrinos, G. Bhanot, S.H. Dairkee, R.W. Davis, S.S. Jeffrey, Single cell profiling of circulating tumor cells: transcriptional heterogeneity and diversity from breast cancer cell lines, *PLoS One* 7 (2012) e33788, <https://doi.org/10.1371/journal.pone.0033788>.
- D.T. Miyamoto, R.J. Lee, S.L. Stott, D.T. Ting, B.S. Wittner, M. Ulman, M.E. Smas, J.B. Lord, B.W. Brannigan, J. Trautwein, N.H. Bander, C.-L. Wu, L.V. Sequist, M.R. Smith, S. Ramaswamy, M. Toner, S. Maheswaran, D.A. Haber, Androgen receptor signaling in circulating tumor cells as a marker of hormonally responsive prostate cancer, *Cancer Discov.* 2 (2012) 995–1003.
- A. Marusy, V. Almendro, K. Polyak, Intra-tumour heterogeneity: a looking glass for cancer? *Nat. Rev. Cancer* 12 (2012) 323–334, <https://doi.org/10.1038/nrc3261>.
- S. Riethdorf, K. Pantel, Advancing personalized cancer therapy by detection and characterization of circulating carcinoma cells, *Ann. N. Y. Acad. Sci.* 1210 (2010) 66–77, <https://doi.org/10.1111/j.1749-6632.2010.05779.x>.
- K. Pantel, M. Otte, Occult micrometastasis: enrichment, identification and characterization of single disseminated tumour cells, *Semin. Cancer Biol.* 11 (2001) 327–337, <https://doi.org/10.1006/scbi.2001.0388>.
- K.-A. Hyun, H.-I. Jung, Advances and critical concerns with the microfluidic enrichments of circulating tumor cells, *Lab Chip* 14 (2014) 45–56, <https://doi.org/10.1039/C3LC50582K>.
- A.M. Thompson, A.L. Paguirigan, J.E. Kreutz, J.P. Radich, D.T. Chiu, Microfluidics for single-cell genetic analysis, *Lab Chip* 14 (2014) 3135, <https://doi.org/10.1039/C4LC00175C>.
- A. Lenshof, T. Laurell, Continuous separation of cells and particles in microfluidic systems, *Chem. Soc. Rev.* 39 (2010) 1203, <https://doi.org/10.1039/b915999c>.
- M. Hejazian, W. Li, N.-T. Nguyen, Lab on a chip for continuous-flow magnetic cell separation, *Lab Chip* 15 (2015) 959–970, <https://doi.org/10.1039/C4LC01422G>.
- T.Z. Jubery, S.K. Srivastava, P. Dutta, Dielectrophoretic separation of bioparticles in microdevices: a review, *Electrophoresis* 35 (2014) 691–713, <https://doi.org/10.1002/elps.201300424>.
- H. Mulvana, S. Cochran, M. Hill, Ultrasound assisted particle and cell manipulation on-chip, *Adv. Drug Deliv. Rev.* 65 (2013) 1600–1610, <https://doi.org/10.1016/j.addr.2013.07.016>.
- A.A.S. Bhagat, H. Bow, H.W. Hou, S.J. Tan, J. Han, C.T. Lim, Microfluidics for cell separation, *Med. Biol. Eng. Comput.* 48 (2010) 999–1014, <https://doi.org/10.1007/s11517-010-0611-4>.
- Y. Chen, P. Li, P.-H. Huang, Y. Xie, J.D. Mai, L. Wang, N.-T. Nguyen, T.J. Huang, Rare cell isolation and analysis in microfluidics, *Lab Chip* 14 (2014) 626, <https://doi.org/10.1039/c3lc90136j>.
- Y. Gao, W. Li, D. Pappas, Recent advances in microfluidic cell separations, *Analyst* 138 (2013) 4714, <https://doi.org/10.1039/c3an00315a>.
- I. Cima, C. Wen Yee, F.S. Iliescu, W. Min Phyo, K. Hon Lim, C. Iliescu, M. Han Tan, Label-free isolation of circulating tumor cells in microfluidic devices: current research and perspectives, *Biomicrofluidics* 7 (2013) 011810, <https://doi.org/10.1063/1.4780062>.
- R. Harouaka, Z. Kang, S.-Y. Zheng, L. Cao, Circulating tumor cells: advances in isolation and analysis, and challenges for clinical applications, *Pharmacol. Ther.* 141 (2014) 209–221, <https://doi.org/10.1016/j.jm.2011.07.011>.
- T.W. Friedlander, G. Premasekharan, P.L. Paris, Looking back, to the future of circulating tumor cells, *Pharmacol. Ther.* 142 (2014) 271–280, <https://doi.org/10.1016/j.pharmthera.2013.12.011>.
- P. Li, Z.S. Stratton, M. Dao, J. Ritz, T.J. Huang, Probing circulating tumor cells in microfluidics, *Lab Chip* 13 (2013) 602–609, <https://doi.org/10.1039/c2lc90148j>.
- H. Yun, K. Kim, W.G. Lee, Cell manipulation in microfluidics, *Biofabrication* 5 (2013) 22001, <https://doi.org/10.1088/1758-5082/5/2/022001>.
- H. Tsutsui, C.-M.M. Ho, Cell separation by non-inertial force fields in microfluidic systems, *Mech. Res. Commun.* 36 (2009) 92–103, <https://doi.org/10.1016/j.mechrescom.2008.08.006>.
- D.R. Gossett, W.M. Weaver, A.J. Mach, S.C. Hur, H.T.K. Tse, W. Lee, H. Amini, D. Di Carlo, Label-free cell separation and sorting in microfluidic systems, *Anal. Bioanal. Chem.* 397 (2010) 3249–3267, <https://doi.org/10.1007/s00216-010-3721-9>.
- C. Jin, S.M. McFaul, S.P. Duffy, X. Deng, P. Tavassoli, P.C. Black, H. Ma, Technologies for label-free separation of circulating tumor cells: from historical foundations to recent developments, *Lab Chip* 14 (2014) 32–44, <https://doi.org/10.1039/c3lc50625h>.
- K.-A.A. Hyun, H.-I. Il Jung, Microfluidic devices for the isolation of circulating rare cells: a focus on affinity-based, dielectrophoresis, and hydrophoresis, *Electrophoresis* 34 (2013) 1028–1041, <https://doi.org/10.1002/elps.201200417>.
- J. Chen, J. Li, Y. Sun, Microfluidic approaches for cancer cell detection, characterization, and separation, *Lab Chip* 12 (2012) 1753, <https://doi.org/10.1039/c2lc21273k>.
- Z.T.F. Yu, K.M. Aw Yong, J. Fu, Microfluidic blood cell sorting: now and beyond, *Small* 10 (2014) 1687–1703, <https://doi.org/10.1002/sml.201302907>.
- L. Hajba, A. Guttman, Circulating tumor-cell detection and capture using microfluidic devices, *TrAC Trends Anal. Chem.* 59 (2014) 9–16, <https://doi.org/10.1016/j.trac.2014.02.017>.
- A.A.S. Bhagat, S.S. Kuntaegodanahalli, I. Papatrsky, Inertial microfluidics for continuous particle filtration and extraction, *Microfluidics. Nanofluidics.* 7 (2009) 217–226, <https://doi.org/10.1007/s10404-008-0377-2>.
- J. Zhang, M. Li, W.H. Li, G. Alici, Inertial focusing in a straight channel with asymmetrical expansion–contraction cavity arrays using two secondary flows, *J. Micromech. Microeng.* 23 (2013) 085023, <https://doi.org/10.1088/0960-1317/23/8/085023>.
- X. Wang, M. Zandi, C.-C. Ho, N. Kaval, I. Papatrsky, Single stream inertial focusing in a straight microchannel, *Lab Chip* 15 (2015) 1812–1821, <https://doi.org/10.1039/c4lc01462f>.
- B.L. Khoo, M.E. Warkiani, D.S.W. Tan, A.A.S. Bhagat, D. Irwin, D.P. Lau, A.S.T. Lim, K.H. Lim, S.S. Krisna, W.T. Lim, Y.S. Yap, S.C. Lee, R.A. Soo, J. Han, C.T. Lim, Clinical validation of an ultra high-throughput spiral microfluidics for the detection and enrichment of viable circulating tumor cells, *PLoS One* 9 (2014) 1–7, <https://doi.org/10.1371/journal.pone.0099409>.
- H.W.H. Hou, M.M.E. Warkiani, B.B.L. Khoo, Z.Z.R. Li, R.A.R. Soo, D.S.-W. Tan, W.-T. Lim, J. Han, A.A.S. Bhagat, C.T. Lim, Isolation and retrieval of circulating tumor cells using centrifugal forces, *Sci. Rep.* 3 (2013) 1259, <https://doi.org/10.1038/srep01259>.
- M.E. Warkiani, G. Guan, K.B. Luan, W.C. Lee, A.A.S. Bhagat, P. Kant Chaudhuri, D.S.-W. Tan, W.T. Lim, S.C. Lee, P.C.Y. Chen, C.T. Lim, Slanted spiral microfluidics for the ultra-fast, label-free isolation of circulating tumor cells, *Lab Chip* 14 (2014) 128–137, <https://doi.org/10.1039/C3LC50617G>.
- H. Ramachandriaiah, H.A. Svahn, A. Russon, Inertial microfluidics combined with selective cell lysis for high throughput separation of nucleated cells from whole blood, *RSC Adv.* 7 (2017) 29505–29514, <https://doi.org/10.1039/C7RA02992F>.
- J. Sun, C. Liu, M. Li, J. Wang, Y. Xianyu, G. Hu, X. Jiang, Size-based hydrodynamic rare tumor cell separation in curved microfluidic channels, *Biomicrofluidics* 7 (2013) 011802, <https://doi.org/10.1063/1.4774311>.
- J. Zhang, S. Yan, R. Sluyter, W. Li, G. Alici, N.-T. Nguyen, Inertial particle separation by differential equilibrium positions in a symmetrical serpentine micro-channel, *Nat. Sci. Reports.* 4 (2014) 1–9, <https://doi.org/10.1038/srep04527>.
- J. Zhang, W. Li, M. Li, G. Alici, N.T. Nguyen, Particle inertial focusing and its

- mechanism in a serpentine microchannel, *Microfluidics*. 17 (2014) 305–316, <https://doi.org/10.1007/s10404-013-1306-6>.
- [45] S. Nagrath, L.V. Sequist, S. Maheswaran, D.W. Bell, D. Irimia, L. Ulkus, M.R. Smith, E.L. Kwak, S. Digumarthy, A. Muzikansky, P. Ryan, U.J. Balis, R.G. Tompkins, D.A. Haber, M. Toner, Isolation of rare circulating tumour cells in cancer patients by microchip technology, *Nature* 450 (2007) 1235–1239, <https://doi.org/10.1038/nature06385>.
- [46] F. Fachin, P. Spuhler, J.M. Martel-Foley, J.F. Edd, T.A. Barber, J. Walsh, M. Karabacak, V. Pai, M. Yu, K. Smith, H. Hwang, J. Yang, S. Shah, R. Yarmush, L.V. Sequist, S.L. Stott, S. Maheswaran, D.A. Haber, R. Kapur, M. Toner, Monolithic chip for high-throughput blood cell depletion to sort rare circulating tumor cells, *Sci. Rep.* 7 (2017) 10936, <https://doi.org/10.1038/s41598-017-11119-x>.
- [47] D. Di Carlo, D. Irimia, R.G. Tompkins, M. Toner, Continuous inertial focusing, ordering, and separation of particles in microchannels, *Proc. Natl. Acad. Sci. U. S. A.* 104 (2007) 18892–18899, <https://doi.org/10.1073/pnas.0704958104>.
- [48] J. Zhang, S. Yan, G. Alici, N.-T. Nguyen, D. Di Carlo, W. Li, Real-time control of inertial focusing in microfluidics using dielectrophoresis (DEP), *RSC Adv.* 4 (2014) 62076–62085, <https://doi.org/10.1039/C4RA13075H>.
- [49] C.-H. Hsu, D. Di Carlo, C. Chen, D. Irimia, M. Toner, Microvortex for focusing, guiding and sorting of particles, *Lab Chip* 8 (2008) 2128–2134, <https://doi.org/10.1039/b813434k>.
- [50] X. Wang, J. Zhou, I. Papautsky, Vortex-aided inertial microfluidic device for continuous particle separation with high size-selectivity, efficiency, and purity, *Biomicrofluidics* 7 (2013) 22–25, <https://doi.org/10.1063/1.4818906>.
- [51] E. Sollier, D.E. Go, J. Che, D.R. Gossett, S. O'Byrne, W.M. Weaver, N. Kummer, M. Rettig, J. Goldman, N. Nickols, S. McCloskey, R.P. Kulkarni, D. Di Carlo, Size-selective collection of circulating tumor cells using Vortex technology, *Lab Chip* 14 (2014) 63–77, <https://doi.org/10.1039/c3lc50689d>.
- [52] A. Özbey, M. Karimzadehkhoei, S. Akgönül, D. Gozuacik, A. Koşar, Inertial focusing of Microparticles in Curvilinear Microchannels, *Sci. Rep.* 6 (2016) 1–11, <https://doi.org/10.1038/srep38809>.
- [53] O. Oral, Y. Akkoc, O. Bayraktar, D.G.-H. Histopathol, U. 2016, Physiological and pathological significance of the molecular cross-talk between autophagy and apoptosis, *Histol. Histopathol.* 31 (2016) 479–498.
- [54] S. Yan, D. Yuan, Q. Zhao, J. Zhang, W. Li, The continuous concentration of particles and cancer cell line using cell margination in a groove-based channel, *Micromachines*. 8 (2017) 315, <https://doi.org/10.3390/mi8110315>.
- [55] U.M. Warawdekar, V. Parmar, A. Prabhu, A. Kulkarni, M. Chaudhari, R.A. Badwe, A versatile method for enumeration and characterization of circulating tumour cells from patients with breast cancer, *J. Cancer Metastasis Treat.* 3 (2017) 23, <https://doi.org/10.20517/2394-4722.2016.66>.
- [56] G. Wang, *Microfluidic Cell Separation Based on Cell Stiffness*, (2014).
- [57] M.M. Ferreira, V.C. Ramani, S.S. Jeffrey, Circulating tumor cell technologies, *Mol. Oncol.* 10 (2016) 374–394, <https://doi.org/10.1016/j.molonc.2016.01.007>.
- [58] B.L. Khoo, S.C. Lee, P. Kumar, T.Z. Tan, M.E. Warkiani, S.G.W. Ow, S. Nandi, C.T. Lim, J.P. Thiery, Short-term expansion of breast circulating cancer cells predicts response to anti-cancer therapy, *Oncotarget* 6 (2015) 15578–15593, <https://doi.org/10.18632/oncotarget.3903>.
- [59] P. Li, Z. Mao, Z. Peng, L. Zhou, Y. Chen, P.-H. Huang, C.I. Truica, J.J. Drabick, W.S. El-Deiry, M. Dao, S. Suresh, T.J. Huang, Acoustic separation of circulating tumor cells, *Proc. Natl. Acad. Sci. U. S. A.* 112 (2015) 4970–4975, <https://doi.org/10.1073/pnas.1504484112>.
- [60] C.-L. Chang, W. Huang, S.I. Jalal, B.-D. Chan, A. Mahmood, S. Shahda, B.H. O'Neil, D.E. Matei, C.A. Savran, Circulating tumor cell detection using a parallel flow micro-aperture chip system, *Lab Chip* 15 (2015) 1677–1688, <https://doi.org/10.1039/C5LC00100E>.
- [61] K. Louterback, J. D'Silva, L. Liu, A. Wu, R.H. Austin, J.C. Sturm, Deterministic separation of cancer cells from blood at 10 mL/min, *AIP Adv.* 2 (2012) 042107, <https://doi.org/10.1063/1.4758131>.
- [62] L. Zhao, C.D. Kroenke, J. Song, D. Piwnica-Worms, J.J.H. Ackerman, J.J. Neil, Intracellular water-specific MR of microbead-adherent cells: the HeLa cell intracellular water exchange lifetime, *NMR Biomed.* 21 (2008) 159–164, <https://doi.org/10.1002/nbm.1173>.
- [63] S.J. Tan, L. Yobas, G.Y.H. Lee, C.N. Ong, C.T. Lim, Microdevice for the isolation and enumeration of cancer cells from blood, *Biomed. Microdevices* 11 (2009) 883–892, <https://doi.org/10.1007/s10544-009-9305-9>.
- [64] M.J. Rosenbluth, W.A. Lam, D.A. Fletcher, Force microscopy of nonadherent cells: a comparison of leukemia cell deformability, *Biophys. J.* 90 (2006) 2994–3003, <https://doi.org/10.1529/BIOPHYSJ.105.067496>.
- [65] J. Zhang, S. Yan, D. Yuan, G. Alici, N.-T. Nguyen, M. Ebrahimi Warkiani, W. Li, Fundamentals and applications of Inertial microfluidics: a review, *Lab Chip* 16 (2016) 10–34, <https://doi.org/10.1039/C5LC01159K>.
- [66] H. Amini, W. Lee, D. Di Carlo, D. Di Carlo, D. Di Carlo, Inertial microfluidic physics, *Lab Chip* 14 (2014) 2739–2761, <https://doi.org/10.1039/c4lc00128a>.
- [67] D.R. Gossett, D. Di Carlo, D. Di Carlo, Particle focusing mechanisms in curving confined flows, *Anal. Chem.* 81 (2009) 8459–8465, <https://doi.org/10.1021/ac901306y>.
- [68] E.E.S. Asmolov, The inertial lift on a spherical particle in a plane Poiseuille flow at large channel Reynolds number, *J. Fluid Mech.* 381 (1999) 63–87, <https://doi.org/10.1017/S0022112098003474>.
- [69] S.C. Hur, S.-E. Choi, S. Kwon, D. Di Carlo, Inertial focusing of non-spherical microparticles, *Appl. Phys. Lett.* 99 (2011) 044101, <https://doi.org/10.1063/1.3608115>.
- [70] M. Masaeli, E. Sollier, H. Amini, W. Mao, K. Camacho, N. Doshi, S. Mitragotri, A. Alexeev, D. Di Carlo, Continuous inertial focusing and separation of particles by shape, *Phys. Rev. X* 2 (2012) 031017, <https://doi.org/10.1103/PhysRevX.2.031017>.
- [71] S.C. Hur, N.K. Henderson-MacLennan, E.R.B. McCabe, D. Di Carlo, Deformability-based cell classification and enrichment using inertial microfluidics, *Lab Chip* 11 (2011) 912, <https://doi.org/10.1039/c0lc00595a>.